Please do not adjust margins

This is the Pre-Published Version.

ARTICLE

Memristor based on 2D $MoSe_2$ nanosheets as artificial synapse and nociceptor for neuromorphic computing

Received 00th January 20xx,
Accepted 00th January 20xx

DOI: 10.1039/x0xx00000x

Huan Duan,[a] Dehui Wang,[a] Jingxi Gou,[a] Feng Guo,[b,c] Wenjing Jie*[a] and Jianhua Hao*[b,c]

Neuromorphic computing inspired by the human brain is highly desirable in the artificial intelligence age. Thus, it is essential to comprehensively investigate the neuromorphic characteristics of artificial synapse and neurons which are the unit cells in the artificial neural network (ANN). Memristor is considered to be an ideal candidate to serve as artificial synapse and neurons in the ANN. Herein, two-terminal memristors based on two-dimensional (2D) $MoSe_2$ nanosheets are fabricated, demonstrating analog resistive switching (RS) behaviors. Unlike the digital RS behaviors with the sharp transition between the two resistance states, the analog RS provides a series of tunable resistance states, which is more suitable for the realization of synaptic plasticity. Thus, the fabricated memristors successfully implement the synaptic functions, such as paired-pulse facilitation, long-term potentiation and long-term depression. The analog memristors can be utilized to construct the ANN for image recognition, leading to the high recognition accuracy of 92%. In addition, the synaptic memristors can emulate the "learning-forgetting" experience of human brain. Furthermore, to demonstrate the ability of single neuron learning in our devices, the memristors are studied as an artificial nociceptor to recognize noxious stimuli. Our research provides comprehensive investigations on the neuromorphic characteristics of artificial synapses and nociceptors, suggesting a promising prospect for applications in neuromorphic computing based on 2D $MoSe_2$ nanosheets.

Introduction

With the increasing need for rapid development of artificial intelligence (AI), the traditional Von Neumann architecture with the separation of memory and computing unit is challenged.[1,2] Neuromorphic computing inspired by the human brain can eliminate the barrier and provide an efficient alternative for bioinspired in-memory computing.[3] Memristors have demonstrated enormous potential for applications in such brain-like neuromorphic computing by utilizing the simultaneous realization of memory and computing in one device.[4-6] Moreover, memristor with synaptic functions is considered to be an ideal candidate to construct the artificial neural network (ANN).[7-9] Recently, memristors based on two-dimensional (2D) materials have received much attention in simulating synaptic functions.[10,11] Transition metal dichalcogenides (TMDCs) as the typical 2D materials have been widely studied in memristive devices.[12,13] For example, gate-tunable MoS_2 memristor was reported in 2015 and MoS_2 synapse with ultra-low variability and implementation in Boolean logic was achieved in 2022.[14,15] On the other hand, the resistive switching (RS) properties of $MoSe_2$ have been constantly studied recently. In 2015, Yan et al. reported the RS properties of $MoSe_2$ nanorods.[16] The light-controlled RS behavior was observed by Han et al. in 2016.[17] The temperature-controlled RS behavior was reported by Li et al. in 2017.[18] In 2019, Wang et al. reported a memristor based on a $MoSe_2/Bi_2Se_3$ heterostructure.[19] The device achieved threshold switching behaviors and emulated synaptic plasticity under near-infrared irradiation. In 2021, Jian et al. synthesized $MoSe_2$ clusters by hydrothermal method and fabricated memristors with low SET/RESET voltage of 0.5/− 0.75 V.[20] In 2022, Liu et al. constructed a $MoSe_2/MoS_2$ heterostructure which exhibited good bipolar RS behaviors and emulated synaptic plasticity.[21] Very recently, Bala et al. constructed a $Mo/MoSe_{(x<2)}/MoSe_2$ stacking structure in which excellent RS properties were realized by using controlled diffusion of Se.[22]

As a RS layer in memristive devices, $MoSe_2$ exhibited marvelous RS behaviors, offering a promising prospect for applications in synaptic device. And more importantly, memristors have been recently studied not only as artificial synapses for potential applications in neuromorphic computing, but also as single neuron, such as artificial nociceptors to recognize noxious stimuli for applications in AI and in-memory computing.[23] Acting as a unique receptor of sensory neurons, nociceptors can recognize noxious stimuli above a pre-set noxious threshold, and then warn the central nervous system and decrease the threshold,[24,25] which is different from some general sensory receptors that typically decrease their sensitivity after subjected to external stimuli for a long time. At current stage, artificial nociceptors are seldom reported based on 2D layered nanosheets.[26,27] Considering the suitable RS behaviors of $MoSe_2$ in synaptic devices, it is meaningful to explore the synaptic

[a.] College of Chemistry and Materials Science, Sichuan Normal University, Chengdu, 610066, China.
[b.] Department of Applied Physics, The Hong Kong Polytechnic University, Hong Kong, 999077, China.
[c.] The Hong Kong Polytechnic University Shenzhen Research Institute, Shenzhen, 518057, China.
*. Email: wenjing.jie@sicnu.edu.cn; jh.hao@polyu.edu.hk.

Please do not adjust margins

Please do not adjust margins

functions, neuromorphic computing and nociceptive emulators based on 2D $MoSe_2$ nanosheets.

In this work, we synthesized 2D $MoSe_2$ nanosheets by the salt-assisted chemical vapor deposition (CVD) method and prepared two-terminal Pt/$MoSe_2$/Pt memristors with analog RS behavior which is very conducive to the realization of synaptic plasticity. The fabricated memristors demonstrated various synaptic functions, such as short-term plasticity represented by paired-pulse facilitation (PPF) and long-term plasticity represented by long-term potentiation (LTP) and long-term depression (LTD). Based on the synaptic memristor, three-layer ANN can be constructed and the image recognition accuracy can reach up to 92%. In addition, the synaptic memristor can be used to simulate the "learning-forgetting" experience of human brain. More importantly, the device can serve as an artificial nociceptor to recognize noxious stimuli, suggesting potential applications in future for in-memory computing and AI.

Experimental

Material Synthesis

The hexagonal 2D layered $MoSe_2$ nanosheets were synthesized on SiO_2/Si substrates by salt-assisted CVD method, as schematically shown in Fig. 1a. Selenium (Se) and molybdenum trioxide (MoO_3) powders were used to provide Se and Mo sources, respectively. Potassium chloride (KCl) was added as a catalyst mixed with MoO_3 to lower its melting point. The CVD growth was carried out in a tube furnace with two independent temperature zones where a gas mixture of 90% argon (Ar) and 10% hydrogen (H_2) was employed as the carrier gas with the gas flow rate of 60 standard cubic centimeters per minute (sccm). During the experiment, 200 mg of Se powders were placed on the upstream side of tube furnace and then heated to 350 °C. While, 100 mg of MoO_3 powders mixed with KCl were placed 17 cm downstream from the Se powder and heated to 750 °C for growth. After 12-min reaction, the furnace was cooled naturally to room temperature.

Device Fabrication

hexagonal 2D layered $MoSe_2$ nanosheets were achieved on SiO_2/Si substrates. Two-terminal Pt/$MoSe_2$/Pt horizontal device was fabricated through the standard photolithography technique. Firstly, the synthesized $MoSe_2$ nanosheets were transferred onto the target SiO_2/Si substrate for device fabrication. Then, the electrode patterns were well prepared directly on the $MoSe_2$ nanosheets by photolithography. After that, 100 nm Pt thin film was deposited as the electrodes by sputtering method. Then, the redundant photoresist and Pt were removed by ultrasonic cleaning with acetone. Finally, the Pt/$MoSe_2$/Pt devices were dried at 100 °C for 1 min on a heater.

Characterizations and Measurements

Atomic force microscopy (AFM, Asylum Research MFP-3D) was used to characterize the thickness and surface morphology of the synthesized $MoSe_2$ nanosheets. Photoluminescence (PL) and Raman characterizations were performed using a high-resolution confocal-Raman/PL system (Witec alpha 300 R) with a 532 nm laser source. All electrical tests were performed using the double channel Keithley 2636B source meter equipped with a home-made four-probe station system at room temperature in air. A three-layer ANN was constructed based on a software algorithm to recognize handwritten digits of small images with 8 × 8 pixels from the dataset of Optical Recognition of Handwritten Digits and large images with 28 × 28 pixels from the dataset of Modified National Institute of Standards and Technology (MNIST). The neural network simulations were performed through CrossSim platform. According to the back propagation algorithm, the program code was written in Python.

Results and discussion

2D $MoSe_2$ nanosheets with hexagonal shape can be successfully synthesized by the CVD method, as shown in the optical image Fig. 1b. AFM image (Fig. 1c) suggests that the $MoSe_2$ nanosheet possesses a smooth surface and the thickness is of ~ 1.9 nm. It is approximately two unit layers by considering the 0.8 nm thickness of monolayer $MoSe_2$ nanosheet.[28,29] Fig. 1d shows the Raman spectrum of the synthesized $MoSe_2$ nanosheets. There are two Raman characteristic peaks located at 238.3 cm^{-1} and 285.4 cm^{-1}, corresponding to out-of-plane A_{1g} and in-plane E_{2g} mode, respectively.[30,31] In particular, a characteristic peak located at 248.4 cm^{-1} may be caused by the Se vacancies, which was reported in previous work.[30] Fig. 1e and 1f show the A_{1g} intensity of Raman mapping image and emission peak intensity of PL mapping image of the hexagonal nanosheet indicated by the white dashed line in Fig. 1b, respectively. Clear and homogeneous hexagonal morphology can be observed in both mapping images, suggesting the 2D $MoSe_2$ nanosheet can be synthesized by the salt-assisted CVD method. The inset of Fig. 1f shows the PL spectrum of the $MoSe_2$ nanosheet with an intense emission peak located at 790 nm, which can be ascribed to the direct bandgap emission of A-exciton.[31]

For the RS performance measurements, two-terminal Pt/$MoSe_2$/Pt device has been fabricated, as schematically shown in Fig. 2a. Fig. S1 shows the optical microscope image of the memristor with the channel length of 5 μm. The current−voltage (*I*−*V*) curve of Pt/$MoSe_2$/Pt device is demonstrated in Fig. 2b. A hysteresis loop under continuous direct current (DC) voltage sweeping (with the scanning direction: 0 V → 5 V → 0 V → − 5 V → 0 V) can be observed for the device without the electroforming process. The device exhibits analog RS behavior, which is suitable for synaptic functions compared with digital RS in which a sharp transition from the high to low resistance state can be observed.[32,33] When a series of consecutive positive voltage sweepings (0 V → 5 V → 0 V) are applied to the device, the current increases with the increase of scanning times, as shown in Fig. 2c. The observed analog RS behaviors can be ascribed to the existence of Se vacancies which can be confirmed by the Raman spectrum (Fig. 1d). The absence of the sharp transition from the high to low resistance state suggests that conductive bridges can not be formed to connect the two electrodes. However, the Se vacancies may form some discrete conductive filaments which can slightly decrease the resistance of the device and consequently give rise to the observed

This journal is © The Royal Society of Chemistry 20xx

Please do not adjust margins

Please do not adjust margins

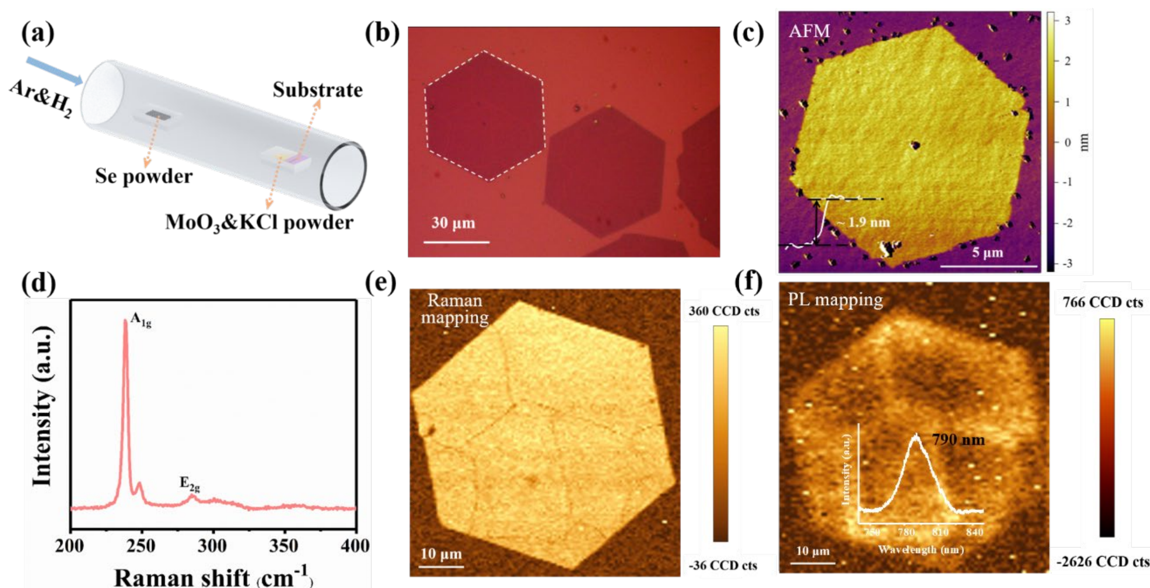

Fig. 1 Characterizations of $MoSe_2$ nanosheets synthesized by the salt-assisted CVD method. (a) Schematic of the salt-assisted CVD growth process. (b) Optical image of the synthesized hexagonal $MoSe_2$ nanosheets on SiO_2/Si substrate. (c) AFM image of a typical $MoSe_2$ flake. (d) Typical Raman spectrum of the $MoSe_2$ flake indicated by the white dash line in (b). (e) Intensity mapping image of A_{1g} mode for the $MoSe_2$ flake indicated by the white dash line in (b). (f) Intensity mapping image of the emission peak for the $MoSe_2$ flake indicated by the white dash line in (b). Inset is a typical PL spectrum of the flake.

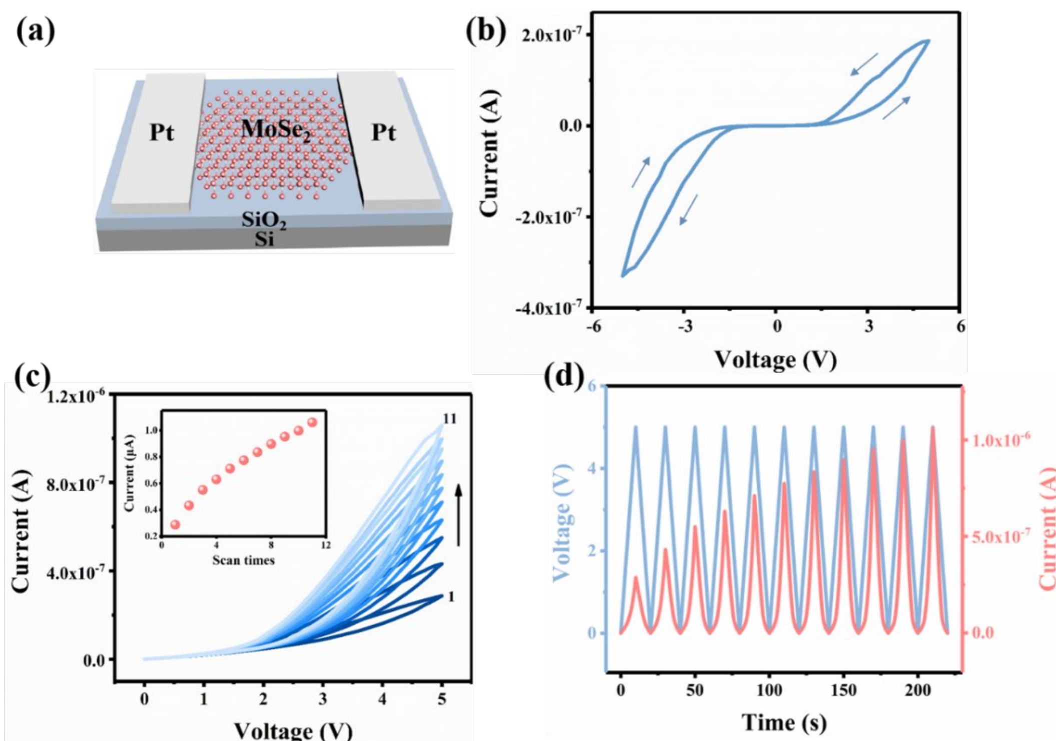

Fig. 2 RS performance of the Pt/$MoSe_2$/Pt memristor. (a) Schematic of the fabricated two-terminal memristor. (b) The typical *I*–*V* curve of the memristor. (c) The *I*–*V* curves of the memristor for a series of consecutive (11 times) positive voltage sweepings (0 V → 5 V → 0 V). The inset shows the current value at 5 V as a function of the sweeping times (from the 1st to the 11th). (d) The current and the applied DC sweeping voltage as a function of time.

increase of current as the sweeping times.[34-36] When a positive voltage is applied to the device, the selenium vacancies gradually migrate to the opposite electrode and shorten the distance between the two electrodes, resulting in the gradual increase of current. The inset in Fig. 2c shows that the current value at 5 V increase with the sweeping times. The current of the device at 5 V increases steadily as the sweeping times increase, suggesting the potentiation effects of the positive voltages. The variation of current and the applied sweeping voltages with time is shown in Fig. 2d. It is obvious that the current gradually increases as the scanning time increase in the same scanning voltage scale.

Please do not adjust margins

Please do not adjust margins

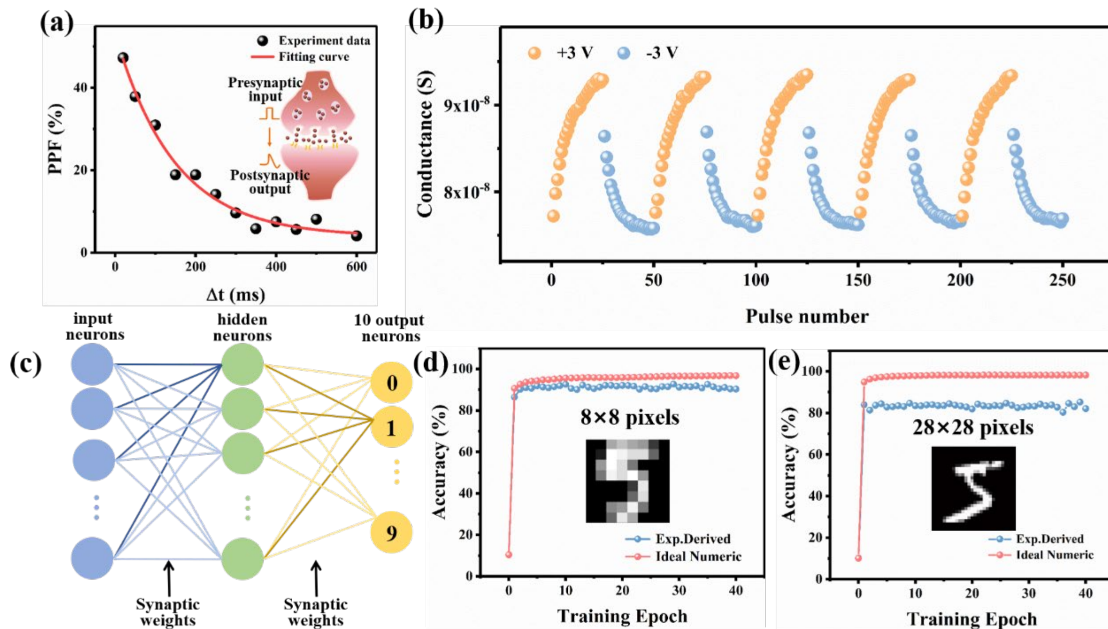

Fig. 3 Neuromorphic computing based on the synaptic memristor. (a) PPF index as a function of the time interval between two sequential pulses. Inset shows the schematic of an artificial synapse. (b) Repeatable 5 sets of LTP-LTD circles. (c) The schematic of the three-layer ANN. The training results for image recognition of the small dataset (d) and large dataset (e).

The devices with analog switching behaviors are highly desirable for applications in artificial synapse. A synapse, as schematically shown in the inset of Fig. 3a, consists of the presynaptic membrane, the synaptic gap and the postsynaptic membrane, which plays the role for information transfer between two neurons.[37] The presynaptic membrane releases neurotransmitters that can be accepted by the postsynaptic membrane. Synaptic plasticity refers to the temporal correlation of synaptic weights after different stimuli.[38,39] An artificial synapse is capable of responding dynamically to external successive stimuli. The synaptic weights in an artificial synapse can be indicated by the postsynaptic current (PSC). The PPF is a typical type of the short-term plasticity.[33] When stimulated by two successive voltage pulses, an enhancement effect of the former stimulus on the latter one can be observed. Fig. 3a shows the PPF index as a function of the pulse interval (Δt) when the artificial synapse is stimulated by two consecutive voltage pulses with the pulse amplitude (V) of 1.5 V and width (W) of 50 ms. The PPF index can be described as $(A_2 - A_1)/A_1 \times 100\%$, where A_1 and A_2 are the PSCs after the first and the second pulse stimulation, respectively.[13,40] The PPF index can be fitted to show an exponential decay with the Δt, which is consistent with the biological synaptic behavior. Furthermore, the long-term plasticity of LTP and LTD are studied when the device is stimulated by 25 consecutive positive voltage pulses (V = 3 V, W = 50 ms, Δt = 50 ms) followed by 25 negative voltage pulses (V = − 3 V, W = 50 ms, Δt = 50 ms). Fig. 3b shows the 5 cycles of the LTP and LTD with good repeatability. For positive voltage pulses, the device conductance is gradually increased, corresponding to the LTP, which is consistent with the potentiation behaviors under consecutive positive DC voltage sweeping. Fig. S2 shows the potentiation behaviors depending on the pulse width. As the pulse width increases from 20 to 80 ms, the potentiation effects are enhanced in the LTP behaviors. For negative voltage pulses, LTD functions can be emulated with the steadily decreased conductance. Next, our synaptic memristors can be used to simulate a three-layer neural network with the input, hidden and output layers, as shown in Fig. 3c. The conductance states of the synaptic memristors are used as a weight update for performing back propagation simulation of neuromorphic computing. The neural network simulations are performed through Crosssim platform. Fig. S3 shows consecutive 20 sets of LTP/LTD circles, suggesting good repeatability of the LTP/LTD for image recognition. Furthermore, to describe the linearity of LTP and LTD quantitatively, the LTP and LTD curves are fitted (as shown in Fig. S4), suggesting relatively good linearity of the LTP and LTD. With good repeatability and linearity in the LTP and LTD behaviors, the constructed ANN based on a software algorithm can be trained to recognize handwritten digits of small images with 8 × 8 pixels and large images with 28 × 28 pixels.[41,42] The recognition accuracy of our device can reach up to 92% for the small images, as shown in Fig. 3d. The variation of recognition accuracy with training cycles for large images is depicted in Fig. 3e. The recognition accuracy can reach up to 85% for the large images, suggesting the potential applications in neuromorphic computing based on our synaptic memristor with analog RS behaviors.

Furthermore, our synaptic device is also capable of simulating the “learning-forgetting” process of the human brain. Fig. 4a shows three successive “learning-forgetting” processes where 25 consecutive positive voltage pulses (V = 4 V, W = 50 ms, Δt = 50 ms) are employed to stimulate the device followed by the decay process of the current after removing the pulses. The current of the device gradually increases, which is analogous to the learning process of the human brain by considering the cognitive level can be enhanced by the

Please do not adjust margins

Please do not adjust margins

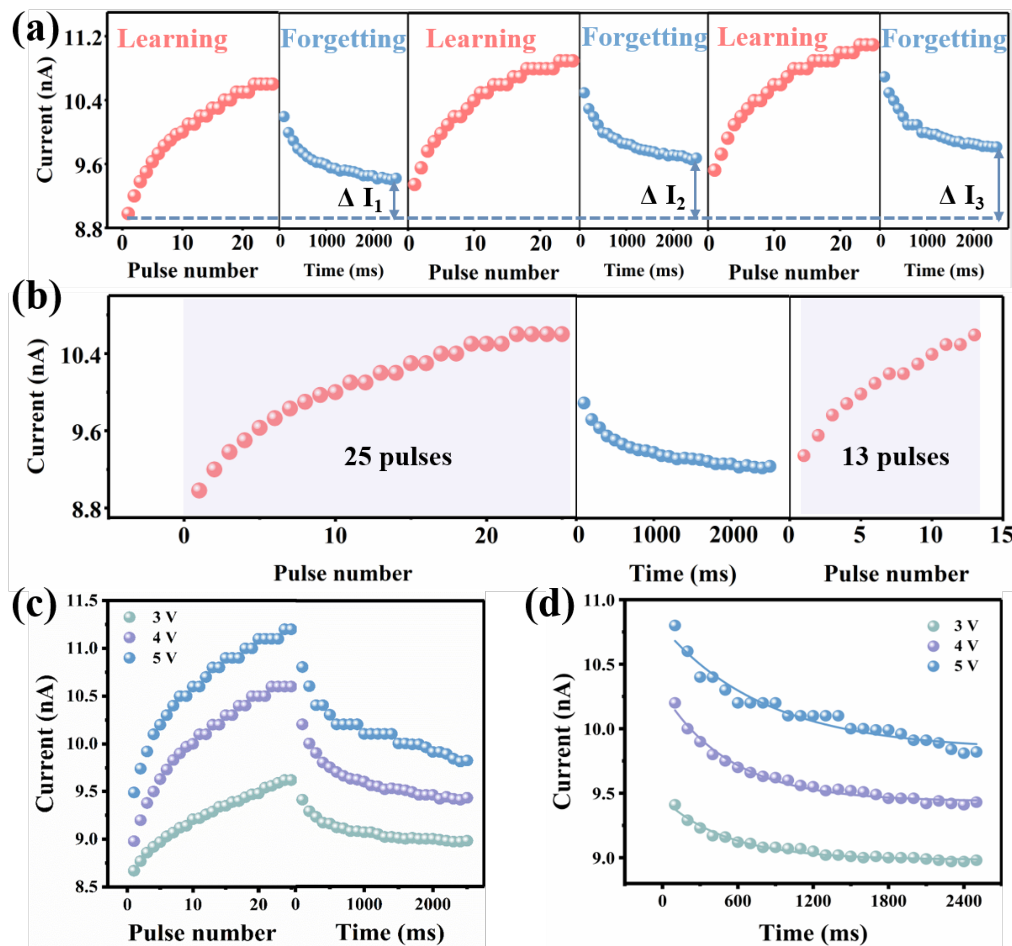

Fig. 4 The "learning-forgetting" process based on the Pt/$MoSe_2$/Pt memristor. (a) The "learning-forgetting" process of three cycles. (b) Detailed view of the first two cycles in (a). (c) The "learning-forgetting" curve with pulse amplitude of 3, 4 and 5 V respectively. (d) The fitted forgetting curves with pulse amplitude of 3, 4 and 5 V, respectively.

learning process. After removing the voltage pulses, the current demonstrates a decay process analogous to the forgetting process. It should be mentioned that the current does not recover to the initial level (before learning) after the decay process of 2500 ms. Through the "learning-forgetting" process, the current increased by ΔI_1, as indicated in Fig. 4a. And more importantly, the increased current is steadily enhanced after the subsequent second and third "learning-forgetting" process, i.e. $\Delta I_3 > \Delta I_2 > \Delta I_1$, implying the cognitive level can be further enhanced by the relearning process. Typically, the "learning-forgetting" process can be introduced by the Ebbinghaus Forgetting Curve where the cognitive level is enhanced by repetitive learning, which is analogous to previously reported "learning-forgetting" processes.[43,44] Fig. 4b shows a detailed view of the first two "learning-forgetting" processes of Fig. 4a. It can be clearly seen that only 13 pulses are needed in the relearning process when the same cognitive level can be reached in the first learning process where 25 pulses are needed. This suggests that less time is needed for the relearning process to achieve same learning effects to the first learning process, which is consistent with the human learning experience. Fig. 4c shows the "learning-forgetting" process stimulated by voltages pulses with different amplitudes of 3, 4 and 5 V. The higher the pulse amplitude, the higher the current level can be reached, suggesting higher learning intensity can generate higher cognitive level. Moreover, after removing the pulses, higher current level can be retained for the higher pulse magnitude in the forgetting process. This fits well with the fact that the higher intensity of learning, the higher cognitive level that can be eventually achieved after same forgetting time. To describe the forgetting process quantitatively, the three forgetting curves in Fig. 4c were fitted using the exponential decay function $I_{(t)} = I_o + Ae^{-t/\tau}$, where I is the recorded current, I_0 is the initial current of decay, A is the pre-factor, and τ is the relaxation time,[45] as illustrated in Fig. 4d. The relaxation time τ is 512, 540 and 826 ms when the pulse amplitude is 3, 4 and 5 V, respectively. The amplitude dependent "learning-forgetting" process indicates that a better learning effect (higher current level) and a longer forgetting time (larger relaxation time) can be obtained by a higher learning intensity (higher the pulse amplitude). Thus, the synaptic device is capable of simulating the "learning-forgetting" experience of human brain.

Moreover, the synaptic device can be used to implement the emulation of nociceptor, as schematically illustrated in Fig. 5a.

Please do not adjust margins

Please do not adjust margins

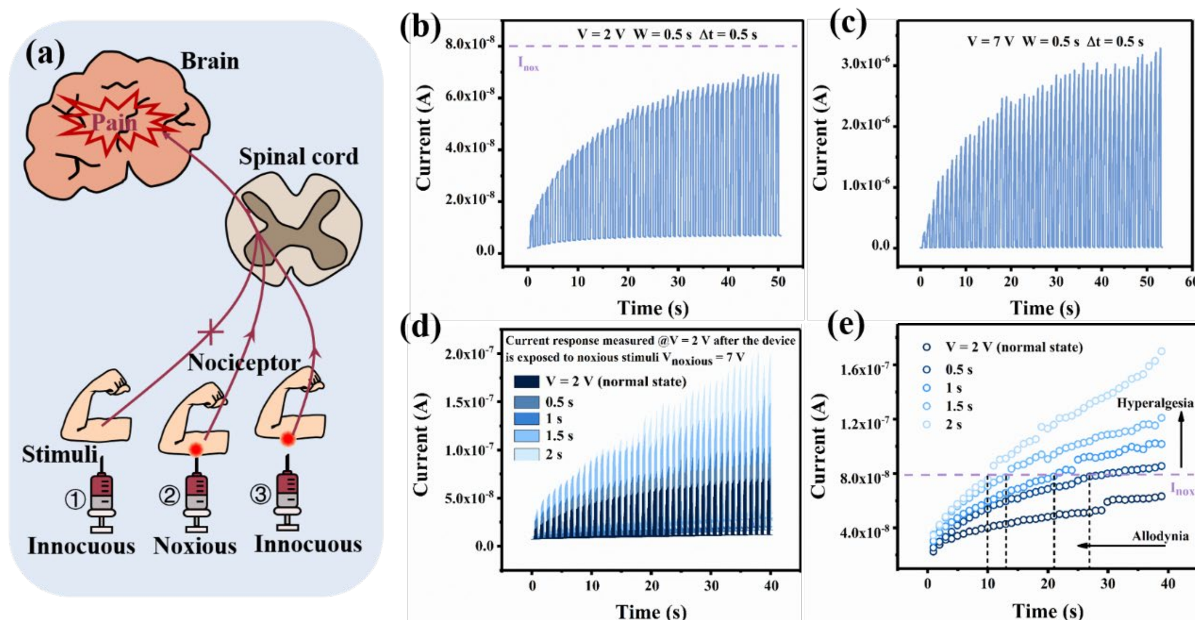

Fig. 5 The emulation of nociceptor based on the synaptic memristor. (a) Schematic of the nociceptor when stimulated by the innocuous and noxious stimuli as well as the innocuous stimulus after a noxious stimulus. (b) The current response of the device to the innocuous stimuli with the V = 2 V. (c) The current response of the device to the noxious stimuli with the V = 7 V. (d) The current response of the device to the innocuous stimuli with the V = 2 V after the device is respectively subjected to the noxious stimuli with different pulse width (0.5, 1, 1.5 and 2 s, V = 7 V). (e) Extraction of spike current value to clearly show the emulation of nociceptor.

Acting as a unique receptor of sensory neurons, nociceptors can be used to detect noxious stimuli, such as external injury and high temperature.[46] The nociceptor can recognize noxious stimuli above a pre-set noxious threshold, and then warn the central nervous system via generation of action potentials, initiate decreasing the threshold and increasing the sensitivity.[24] It should be mentioned that the nociceptor is different from some other sensory receptors, such as sight, hearing, taste, smell, and touch sensory receptors which typically decrease their sensitivity when exposed to external stimuli for a prolonged time. The nociceptors generally decrease their threshold and increase their sensitivity when exposed to external noxious stimuli (such as being hurt by a needle or a knife). For the previous innocuous stimuli, the nociceptors decrease their pain threshold after exposed to external noxious stimuli, which is called "allodynia". The nociceptors increase their response and generate noxious action potentials over the pre-set noxious threshold to the normal innocuous stimuli, which is called "hyperalgesia".[25] Our memristor can be used to serve as an artificial nociceptor. Firstly, 80 nA is defined as the pain threshold (I_{nox} = 80 nA), which means that the pain can be recognized when the current exceeds 80 nA. As shown in Fig. 5b, the current gradually increase under the stimulations of continuous electrical pulses (V = 2 V, W = 0.5 s and Δt = 0.5 s). But the current can not exceed I_{nox} when exposed to the innocuous stimuli of 2 V. In Fig. 5c, the current exceeds I_{nox} at the beginning when exposed to the noxious stimuli of electrical pulses with amplitude of 7 V. After the exposure to the noxious stimuli of 7 V, we investigate the current response of the device to the previous innocuous stimuli of 2 V, as shown in Fig. 5d. The device is exposed to the noxious stimuli of 7 V with different pulse width (0.5, 1, 1.5 and 2 s), after which the device is subjected to previously innocuous stimuli of 2 V. In this case, all the current values exceed I_{nox} after the device is exposed to noxious stimuli. The increased pulse width of the noxious stimuli decreases the incubation time which is the time taken to exceed the I_{nox}. Fig. 5e is plotted by extracting the current values of Fig. 5d. It can be observed that the longer pulse width of the noxious stimuli of 7 V subjected to the device, the shorter incubation time taken for the innocuous stimuli of 2 V. The incubation time is 27, 21, 13 and 10 s for the noxious stimuli with pulse width of 0.5, 1, 1.5 and 2 s, respectively. In addition, the broader the pulse width of the applied noxious stimulus, the more severe of the injuries. Thus, our memristor can be used to well simulate the biological nociceptor.

Conclusions

In summary, based on the Pt/$MoSe_2$/Pt memristors with analog RS behaviors, artificial synapses and nociceptors can be emulated. The memristors exhibit excellent analog resistive behavior and show a series of tunable resistive states, which is attributed to the rearrangement of Se vacancies in the 2D nanosheet to form discrete conductive filaments in response to the DC voltage stimulation. Based on the well-repeated LTP-LTD behavior, the synaptic memristors can be used to construct a three-layer ANN with recognition accuracy of up to 92%. Moreover, the device also successfully implements the "learning-forgetting" experience and emulation of artificial nociceptors, providing a new approach to comprehensively investigate the neuromorphic characteristics based on 2D materials.

Please do not adjust margins

Please do not adjust margins

Author Contributions

H. Duan designed and engineered the samples; D. H. Wang and J. X. Gou performed the experiments; F. Guo performed the data analysis; H. Duan wrote the paper with support from W. J. Jie and J. H. Hao; W. J. Jie and J. H. Hao contributed to the theoretical analysis. All authors contributed to the general discussion.

Conflicts of interest

There are no conflicts to declare.

Acknowledgements

This work was supported by the grants from National Natural Science Foundation of China (No. 61974097 and 52233014), Natural Science Foundation of Sichuan (No. 2022NSFSC0521) and Research Grants Council of Hong Kong (AoE/P-701/20).

References

1 S. Ambrogio, P. Narayanan, H. Tsai, R. M. Shelby, I. Boybat, C. di Nolfo, S. Sidler, M. Giordano, M. Bodini, N. C. P. Farinha, B. Killeen, C. Cheng, Y. Jaoudi and G. W. Burr, *Nature*, 2018, **558**, 60–67.

2 W. Zhang, B. Gao, J. Tang, P. Yao, S. Yu, M.-F. Chang, H.-J. Yoo, H. Qian and H. Wu, *Nat. Electron.*, 2020, **3**, 371–382.

3 X. Deng, S. Q. Wang, Y. X. Liu, N. Zhong, Y. H. He, H. Peng, P. H. Xiang and C. G. Duan, *Adv. Funct. Mater.*, 2021, **31**, 2101099.

4 L. Qin, S. Cheng, B. Xie, X. Wei and W. Jie, *Appl. Phys. Lett.*, 2022, **121**, 093502.

5 H. Duan, S. Cheng, L. Qin, X. Zhang, B. Xie, Y. Zhang and W. Jie, *J. Phys. Chem. Lett.*, 2022, **13**, 7130–7138.

6 H. Chen, Y. Kang, D. Pu, M. Tian, N. Wan, Y. Xu, B. Yu, W. Jie and Y. Zhao, *Nanoscale*, 2023, **15**, 4309–4316.

7 X. Zhang, H. Chen, S. Cheng, F. Guo, W. Jie and J. Hao, *ACS Appl. Mater. Interfaces*, 2022, **14**, 44614–44621.

8 K. Liao, P. Lei, M. Tu, S. Luo, T. Jiang, W. Jie and J. Hao, *ACS Appl. Mater. Interfaces*, 2021, **13**, 32606–32623.

9 Y. Yang, H. Du, Q. Xue, X. Wei, Z. Yang, C. Xu, D. Lin, W. Jie and J. Hao, *Nano Energy*, 2019, **57**, 566–573.

10 T. Ohno, T. Hasegawa, T. Tsuruoka, K. Terabe, J. K. Gimzewski and M. Aono, *Nat. Mater.*, 2011, **10**, 591–595.

11 T. Guo, B. Sun, S. Ranjan, Y. Jiao, L. Wei, Y. N. Zhou and Y. A. Wu, *ACS Appl. Mater. Interfaces*, 2020, **12**, 54243–54265.

12 C. Yeon, S. J. Yun, J. Yang, D. H. Youn and J. W. Lim, *Small*, 2018, **14**, 1702747.

13 S. Luo, K. Liao, P. Lei, T. Jiang, S. Chen, Q. Xie, W. Luo, W. Huang, S. Yuan, W. Jie and J. Hao, *Nanoscale*, 2021, **13**, 6654–6660.

14 V. K. Sangwan, D. Jariwala, I. S. Kim, K. S. Chen, T. J. Marks, L. J. Lauhon and M. C. Hersam, *Nat. Nanotechnol.*, 2015, **10**, 403–406.

15 A. Krishnaprasad, D. Dev, S. S. Han, Y. Shen, H. S. Chung, T. S. Bae, C. Yoo, Y. Jung, M. Lanza and T. Roy, *ACS Nano*, 2022, **16**, 2866–2876.

16 Y. Yan, B. Sun and D. Ma, *Chem. Phys. Lett.*, 2015, **638**, 103–107.

17 P. Han, B. Sun, S. Cheng, F. Yu, B. Jiao and Q. Wu, *J. Alloy. Compd.*, 2016, **664**, 619–625.

18 P. Li, B. Sun, X. Zhang, G. Zhou, Y. Xia, L. Gan, Y. Zhang and Y. Zhao, *Mater. Lett.*, 2017, **202**, 13–16.

19 Y. Wang, J. Yang, Z. Wang, J. Chen, Q. Yang, Z. Lv, Y. Zhou, Y. Zhai, Z. Li and S. T. Han, *Small*, 2019, **15**, 1805431.

20 J. Jian, H. Feng, P. Dong, H. Chang, A. Vena and S. Brice, *Adv. Electron. Mater.*, 2021, **8**, 2100905.

21 P. Liu, H. Luo, X. Yin, X. Wang, X. He, J. Zhu, H. Xue, W. Mao and Y. Pu, *Appl. Phys. Lett.*, 2022, **121**, 233501.

22 A. Bala, B. So, P. Pujar, C. Moon and S. Kim, *ACS Nano*, 2023, **17**, 4296–4305.

23 S. Wirth, M. Yanike, L. M. Frank, A. C. Smith, E. N. Brown and W. A. Suzuki, *Science*, 2003, **300**, 1578–1581.

24 X. Xu, E. J. Cho, L. Bekker, A. A. Talin, E. Lee, A. J. Pascall, M. A. Worsley, J. Zhou, C. C. Cook, J. D. Kuntz, S. Cho and C. A. Orme, *Adv. Sci.*, 2022, **9**, 2200629.

25 R. A. John, N. Yantara, S. E. Ng, M. I. B. Patdillah, M. R. Kulkarni, N. F. Jamaludin, J. Basu, Ankit, S. G. Mhaisalkar, A. Basu and N. Mathews, *Adv. Mater.*, 2021, **33**, 2007851.

26 G. Ding, R. S. Chen, P. Xie, B. Yang, G. Shang, Y. Liu, L. Gao, W. A. Mo, K. Zhou, S. T. Han and Y. Zhou, *Small*, 2022, **18**, 2200185.

27 J. H. Yang, S. C. Mao, K. T. Chen and J. S. Chen, *Adv. Electron. Mater.*, 2022, **9**, 2201006.

28 J. C. Shaw, H. Zhou, Y. Chen, N. O. Weiss, Y. Liu, Y. Huang and X. Duan, *Nano Research*, 2015, **7**, 511–517.

29 J. P. B. Silva, C. Almeida Marques, J. A. Moreira and O. Conde, *J. Mater. Chem. C*, 2017, **5**, 10353–10359.

30 S. Wang, G. Wang, X. Yang, H. Yang, M. Zhu, S. Zhang, G. Peng and Z. Li, *Nanomaterials*, 2020, **10**, 75.

31 Y.-H. Chang., W. Zhang., Y. Zhu., Y. Han., J. Pu., J.-K. Chang., W.-T. Hsu., J.-K. Huang., C.-L. Hsu., M.-H. Chiu., T. Takenobu., H. Li., C.-I. Wu., W.-H. Chang., A. T. S. Wee. and L.-J. Li., *ACS Nano*, 2014, **8**, 8582–8590.

32 K. Wang, J. Chen and X. Yan, *Nano Energy*, 2021, **79**, 105453.

33 X. Shan, C. Zhao, X. Wang, Z. Wang, S. Fu, Y. Lin, T. Zeng, X. Zhao, H. Xu, X. Zhang and Y. Liu, *Adv. Sci.*, 2022, **9**, 2104632.

34 S. Cheng, L. Zhong, J. Yin, H. Duan, Q. Xie, W. Luo and W. Jie, *Nanoscale*, 2023, **15**, 4801–4808.

35 K. J. Kwak, J. H. Baek, D. E. Lee, I. H. Im, J. Kim, S. J. Kim, Y. J. Lee, J. Y. Kim and H. W. Jang, *Nano Lett.*, 2022, **22**, 6010–6017.

36 J. Ren, H. Shen, Z. Liu, M. Xu and D. Li, *ACS Appl. Mater. Interfaces*, 2022, **14**, 21141–21149.

37 P. Lei, H. Duan, L. Qin, X. Wei, R. Tao, Z. Wang, F. Guo, M. Song, W. Jie and J. Hao, *Adv. Funct. Mater.*, 2022, **32**, 2201276.

38 J. T. Yang, C. Ge, J. Y. Du, H. Y. Huang, M. He, C. Wang, H. B. Lu, G. Z. Yang and K. J. Jin, *Adv. Mater.*, 2018, **30**, 1801548.

This journal is © The Royal Society of Chemistry 20xx

Please do not adjust margins

Please do not adjust margins

39 S. Chandrasekaran, F. M. Simanjuntak, D. Panda and T.-Y. Tseng, *IEEE T. Electron Dev.*, 2019, **66**, 4722–4726.

40 F. Guo, M. Song, M. C. Wong, R. Ding, W. F. Io, S. Y. Pang, W. Jie and J. Hao, *Adv. Funct. Mater.*, 2021, **32**, 2108014.

41 Y. X. Hou, Y. Li, Z. C. Zhang, J. Q. Li, D. H. Qi, X. D. Chen, J. J. Wang, B. W. Yao, M. X. Yu, T. B. Lu and J. Zhang, *ACS Nano*, 2021, **15**, 1497–1508.

42 B. W. Yao, J. Li, X. D. Chen, M. X. Yu, Z. C. Zhang, Y. Li, T. B. Lu and J. Zhang, *Adv. Funct. Mater.*, 2021, **31**, 2100069.

43 H. Bian, X. Qin, Y. Wu, Z. Yi, S. Liu, Y. Wang, C. D. Brites, L. D. Carlos and X. Liu, *Adv. Mater.*, 2022, **34**, 2101895.

44 O. Kapur, D. Guo, J. Reynolds, Y. Han, R. Beanland, L. Jiang, C. de Groot and R. Huang, *Adv. Electron. Mater.*, 2022, **8**, 2200312.

45 H. Abbas, Y. Abbas, G. Hassan, A. S. Sokolov, Y. R. Jeon, B. Ku, C. J. Kang and C. Choi, *Nanoscale*, 2020, **12**, 14120–14134.

46 M. Kumar, H. S. Kim and J. Kim, *Adv. Mater.*, 2019, **31**, 1900021.

This journal is © The Royal Society of Chemistry 20xx

Please do not adjust margins